ADVANCED FUNCTIONAL MATERIALS
www.afm-journal.de

Highly Ordered Mesoporous Crystalline $MoSe_2$ Material with Efficient Visible-Light-Driven Photocatalytic Activity and Enhanced Lithium Storage Performance

Yifeng Shi, Chunxiu Hua, Bin Li, Xiangpeng Fang, Chaohua Yao, Yichi Zhang, Yong-Sheng Hu,* Zhaoxiang Wang, Liquan Chen, Dongyuan Zhao, and Galen D. Stucky*

Highly ordered mesoporous crystalline $MoSe_2$ is synthesized using mesoporous silica SBA-15 as a hard template via a nanocasting strategy. Selenium powder and phosphomolybdic acid ($H_3PMo_{12}O_{40}$) are used as Se and Mo sources, respectively. The obtained products have a highly ordered hexagonal mesostructure and a rod-like particle morphology, analogous to the mother template SBA-15. The UV-vis-NIR spectrum of the material shows a strong light absorption throughout the entire visible wavelength region. The direct bandgap is estimated to be 1.37 eV. The high surface area $MoSe_2$ mesostructure shows remarkable photocatalytic activity for the degradation of rhodamine B, a model organic dye, in aqueous solution under visible light irradiation. In addition, the synthesized mesoporous $MoSe_2$ possess a reversible lithium storage capacity of 630 mAh g^{-1} for at least 35 cycles without any notable decrease. The rate performance of mesoporous $MoSe_2$ is much better than that of analogously synthesized mesoporous MoS_2, making it a promising anode for the lithium ion battery.

1. Introduction

Inorganic mesoporous solids have found broad applications in many areas, including catalysis, sorption, drug/DNA delivery and energy storage, due to their distinctive properties including tunable mesopore structures, the large internal surface area, as well as their easily functionalized frameworks with well-defined ultrathin nanosturctures.[1–3] Mesoporous silica, carbon and transition metal oxides constitute the vast majority of this family because of better understanding on their chemistry. However, mesoporous non-oxide materials that have diverse physical properties and chemical functionalities are much less reported due to the difficulty in designing controllable sol-gel processes for these materials.[4] Recently, there has been sustained effort to prepare nanoporous metal chalcogenides (sulfide, selenide, and telluride) because of the promising potential applications that come from their combining of nanoporous structure characteristic and semiconductor framework nature.[5–7] The major challenge is to find suitable synthetic techniques that can lead to high quality mesoporous crystalline metal chalcogenide semiconductors.

Various mesostructured metal chalcogenides have been fabricated by solution synthesis method using organic surfactants as structure-directing agents.[6,8–13] However, only in very few special cases, the organic surfactants can be completely removed without destroying the ordered mesostructures.[6,14] Moreover, the obtained samples possess nearly amorphous non-stoichiometric frameworks due to the low temperature synthesis.[6,8–14] All these drawbacks inhibit their applications because the physical properties of semiconductor are dramatically affected by its crystallinity and composition. Nanocasting synthesis is an effective alternate method to fabricate crystalline mesoporous solids by using mesoporous solids as hard templates, which provides stable support for high temperature crystallization.[15–18] Several mesoporous crystalline metal

Prof. Y. F. Shi, B. Li, C. H. Yao
College of Material Chemistry
and Chemical Engineering
Hangzhou Normal University
Hangzhou, Zhejiang 310036, China
E-mail: yfshi@hznu.edu.cn
C. X. Hua, Dr. X. P. Fang, Prof. Y.-S. Hu,
Prof. Z. X. Wang, Prof. L. Q. Chen
Key Laboratory for Renewable Energy
Beijing Key Laboratory for New Energy Materials and Devices
Beijing National Laboratory for Condensed Matter Physics
Institute of Physics, Chinese Academy of Sciences
Beijing 100080, China
E-mail: yshu@aphy.iphy.ac.cn
Y. C. Zhang, Prof. G. D. Stucky
Department of Chemistry and Biochemistry
University of California, Santa Barbara
Santa Barbara, CA 93106, USA
Prof. Y.-S. Hu, Prof. L. Q. Chen
School of Materials Science and Engineering
Chonnam National University
Gwangju 500-757, Republic of Korea
Prof. D. Y. Zhao
Department of Chemistry
Fudan University
Shanghai 200433, China

DOI: 10.1002/adfm.201202144

sulfides, including CdS,[19,20] ZnS,[20] In_2S_3,[20] MoS_2 and WS_2,[21] have been successfully synthesized by nanocasting method using H_2S, thiourea or thioglycol as sulfur sources. However, the corresponding selenide and telluride species, such as H_2Se, H_2Te and selenourea, are quite unstable and not suitable for analogously nanocasting synthesis of metal selenides and tellurides. To the best of our knowledge, no ordered mesoporous crystalline metal selenides and tellurides have been reported.

$MoSe_2$ is an interesting narrow-band-gap semiconductor that has a lamellar crystal structure, whose basic crystal unit is built of Se-Mo-Se sandwich layers. Theoretical band-structure calculation results, confirmed by photoelectron spectroscopy analyses, indicate that the energy gap of $MoSe_2$ (≈1.4 eV) matches the solar spectrum very well.[22,23] It is also reported that $MoSe_2$ possesses very high anti-photocorrosion stability due to the fact that the optical transitions of $MoSe_2$ are between nonbonding metal d states.[22,23] Both of these outstanding features of $MoSe_2$ greatly benefit its potential use in photocatalytic related applications, such as photoelectronchemical solar cells, contamination remediation agents and hydrogen production from water splitting.[24–26] A photoelectrochemical solar cell with efficiency of 12% over $MoSe_2$ material has been reported by Pathak et al., which can be attributed to its appropriate band gap (in the range of 1–2 eV) and high optical absorption property.[27]

Layer structured metal chalcogenides are of great interests in energy storage because their crystal structure can be easily utilized for the reversible storage of hydrogen,[28–33] lithium,[34–39] sodium[38,40] and magnesium[40,41] via electrochemical intercalation, making them good candidates for fuel cell, lithium ion battery (LIB), sodium ion battery and magnesium ion battery applications. Recently, a great amount of research has focused on the synthesis and electrochemical lithium storage behavior of various nanostructured MoS_2 materials due to its high theoretical capacity (670 mAh g^{-1}) and excellent cycling performance.[42–55] However, as a close analogue to the layer structured MoS_2, the electrochemical lithium storage performance of $MoSe_2$ has been little reported.[38,39]

Here we report a nanocasting synthesis of highly ordered mesoporous crystalline $MoSe_2$ by using mesoporous silica SBA-15 as a hard template, phosphomolybdic acid (PMA) and selenium powder as Mo and Se sources, respectively. Selenium powder was gasified by reacting with hydrogen gas flow to form the intermediate product H_2Se, which in turn in situ reduces the PMA to $MoSe_2$ within the mesopore of SBA-15. The mesoporous $MoSe_2$ material was obtained after removing the silica template with a HF aqueous solution. The obtained products possess a highly ordered hexagonal mesostructure and a rod-like particle morphology. UV-vis-NIR spectrum of the as-prepared material shows strong light sorption from 400 to 800 nm. It shows remarkable photocatalytic activity for the degradation of organic compounds in aqueous solution under visible light irradiation. In addition, the lithium storage performance of the material was investigated. A reversible lithium storage capacity of 630 mAh g^{-1} for up to 35 cycles without any notable decrease can be obtained. And it shows much better rate performance than the analogously synthesized mesoporous MoS_2, making it a promising anode candidate for lithium ion batteries.

2. Synthesis of Mesoporous $MoSe_2$ Material

In the synthesis of mesoporous $MoSe_2$, mesoporous silica SBA-15 template with 2D hexagonal patterned cylinder mesopores, was firstly prepared according to the literature report and used as the hard template.[56] Nitrogen sorption analysis reveals that the synthesized SBA-15 have a surface area of 680 m^2 g^{-1}, a pore volume of 1.1 cm^3 g^{-1}, and a mean pore size of 9.2 nm (Supporting Information Figure S1). The PMA molybdenum precursor was filled inside the mesopores of SBA-15 via a solvent evaporation induced capillary condensation process.[21] The obtained PMA@SBA-15 nanocomposite, loaded in a quartz boat, was put in the middle of a quartz tube furnace. Another quartz boat with selenium powder was placed side by side with the former boat in the upstream direction. Then the furnace was heated up to 600 °C at a rate of 2 °C min^{-1} under a hydrogen gas flow (200 mL min^{-1}). During this process, selenium was gasified by reacting with hydrogen to form intermediate product H_2Se.[14] The gaseous H_2Se then reacted with molybdenum precursor to form the crystalline $MoSe_2$ material inside the mesopore of the SBA-15 template. After 6 h reaction, the furnace was cooled down to room temperature. The mesoporous $MoSe_2$ product was obtained after removing the silica template by using 4 wt% HF aqueous solution.

Small-angle X-ray diffraction (XRD) patterns of the prepared mesoporous $MoSe_2$ material (**Figure 1**) shows an intensive diffraction peak at 2 theta value around 1.0° and two broad peaks at 2 theta values around 1.7 and 1.9°, corresponding to the 100, 110 and 200 Bragg diffraction peaks of the *p6mm* mesostructure. The clear and intensive X-ray diffraction peaks reveal the successful mesostructure replication of mesoporous $MoSe_2$ from their mesoporous silica template SBA-15. Compared to the small-angle XRD pattern of SBA-15 (Figure 1), the diffraction peaks of mesoporous $MoSe_2$ are slightly shifted to a higher angle because of the high temperature (600 °C) mesostructure shrinkage. Wide-angle XRD pattern of the obtained $MoSe_2$ material (Figure 1 inset) shows more than nine intensive diffraction peaks in the two theta range of 10–90°, indicating the crystalline nature of the prepared material. All recorded diffraction peaks can be indexed to the hexagonal crystal phase of $MoSe_2$ (JCPDS: 77-1715, namely 2H-$MoSe_2$, Figure 1 inset). When the reaction temperature is decreased below 400 °C, no crystalline

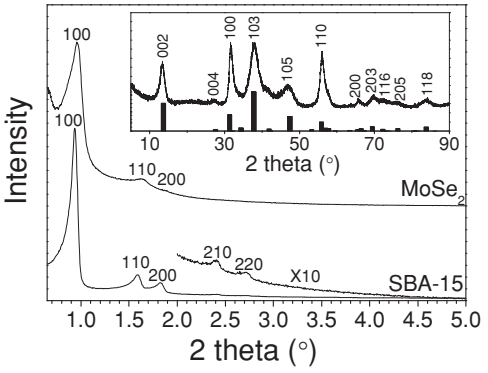

Figure 1. Small-angle XRD patterns of SBA-15 hard template and mesoporous $MoSe_2$ product. Inset: wide-angle XRD pattern of the synthesized mesoporous $MoSe_2$ material.

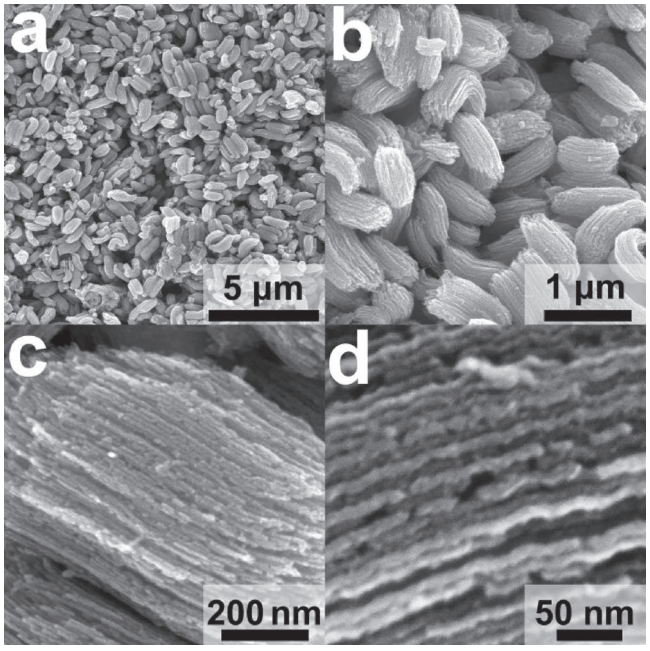

Figure 2. SEM images of the synthesized mesoporous $MoSe_2$ materials using SBA-15 as the template via nanocasting method.

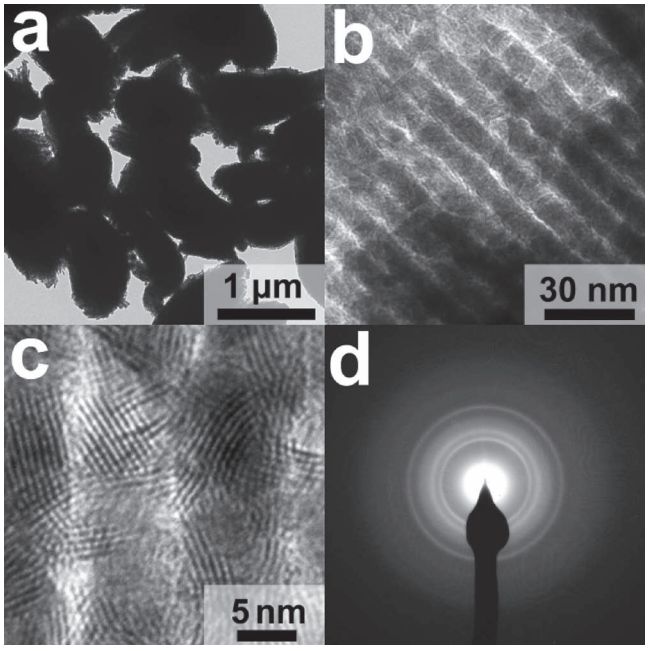

Figure 3. a,b,c) TEM images of ordered mesoporous $MoSe_2$ material and d) its corresponding SAED pattern.

$MoSe_2$ but un-decomposed PMA can be detected in the collected products (Supporting Information Figure S3). Since Se can react with hydrogen to form H_2Se at a temperature as low as 250 °C, the fact that no $MoSe_2$ was formed at 300 °C in our experiment should be attributed to the high thermal stability of PMA. When the synthesis temperature is higher than 400 °C, phase-pure 2H-$MoSe_2$ can be synthesized and no intermediate has been recorded (Supporting Information Figure S3). The crystallinity was slightly increased when the reaction temperature was increased up to 800 °C. However, the XRD patterns still show relatively broad diffraction peaks, indicating the confinement by the limited mesopore of the SBA-15 hard template (9.2 nm, calculated from the nitrogen sorption isotherms as shown in Supporting Information Figure S1).

The mesoporous $MoSe_2$ product was dispersed in ethanol and directly dropped on a sample holder for SEM observation without carbon or gold coating. As shown by the SEM images in **Figure 2**, rod-like particles, ≈1 μm in length and 300–500 nm in diameter, were observed, indicating that it well copied the particle morphology of SBA-15 template (Supporting Information Figure S2). High-resolution SEM images (Figure 2c,d) show that each rod-like particle is composed of an ordered nanowire array. The diameters of these $MoSe_2$ nanowires are estimated to be approximately 8–10 nm as shown in Figure 2d, in agreement with the pore diameter of SBA-15 template's cylindrical mesopore.

TEM observations confirmed that the mesoporous $MoSe_2$ material replicated the rod-like morphology (**Figure 3**a) and the ordered mesostructure (Figure 3b) from its template SBA-15. The HRTEM image (Figure 3c) clearly shows the layered crystal structure with an interlayer distance about 0.65 nm, corresponding to the interplanar distance between the Se-Mo-Se trilayers of 2H-$MoSe_2$. Typical selected area electron diffraction (SAED) pattern of mesoporous $MoSe_2$ (Figure 3d) shows well defined concentric diffraction rings that can be indexed to the 100, 103, 105 and 110 diffractions of $MoSe_2$, indicating its polycrystalline nature. The 002 diffraction ring cannot be recognized in the SAED pattern because it is too close to the primary electron beam image due to the large interplanar distance (≈0.65 nm).

Energy dispersive X-ray (EDX) analysis reveals that the mesoporous $MoSe_2$ product is only composed by molybdenum and selenium (Supporting Information Figure S4). No silicon or oxygen was detected, indicating that the silica template was completely removed and no molybdenum oxide impurities were present in the final product. Nitrogen sorption analysis clearly reveals the mesoporosity of the synthesized $MoSe_2$ sample (Supporting Information Figure S5). The specific surface area, mean pore size, and pore volume derived from the adsorption branch are 55 $m^2\ g^{-1}$, 3.2 nm, and 0.12 $cm^3\ g^{-1}$, respectively. All these values are close to those of analogously synthesized materials with similar mesostructure and bulk density. These results demonstrate that crystalline mesoporous 2H-$MoSe_2$ product has been successfully replicated the ordered mesostructure of the SBA-15 template, as well as the particle morphology.

3. Photocatalytic Degradation of Rhodamine B (RhB)

The UV-vis-NIR absorption spectrum of mesoporous $MoSe_2$ was taken over the spectral range from 250 to 2000 nm as shown in **Figure 4**. The spectrum clearly shows $MoSe_2$ has a strong sorption band covering from 400 to 800 nm, which is the main energy distribution part of the solar spectrum. As for an direct band gap semiconductor, the absorption coefficient α can

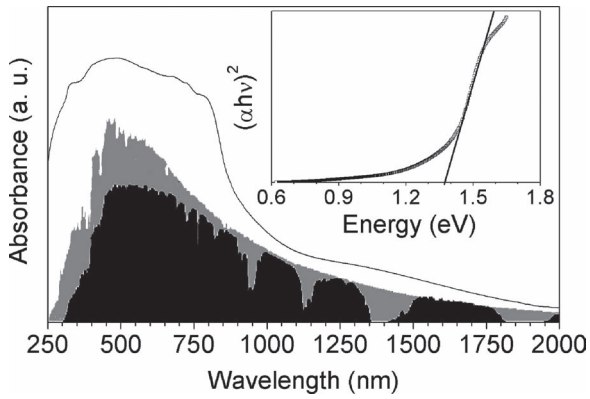

Figure 4. UV-vis-NIR absorption spectrum of the mesoporous $MoSe_2$ material, which matches very well the solar spectrum (gray: top of the atmosphere, black: at sea level). The inset shows the band gap value of the as-prepared material.

be related to photon energy $h\upsilon$ by $(\alpha h\upsilon)^2 = A(h\upsilon - E_g)$, where A is a constant and E_g is the energy band gap. Therefore, the $(\alpha h\upsilon)^2$ versus $h\upsilon$ characteristic is expected to be a straight line with a photoenergy axis intercept indicative for the band gap E_g value of the semiconductor. The inset of Figure 4 illustrated the $(\alpha h\upsilon)^2$ versus $h\upsilon$ lines of mesoporous $MoSe_2$, obtained from its UV-vis-NIR spectrum. The band gap was then estimated from extrapolating the linear portion to the energy axis. The allowed direct band gap is calculated as 1.37 eV, which are in well agreement with earlier reported values for bulk materials, indicating no notable nanoconfinement effect in this material.[57,58]

The photocatalytic activity for the synthesized $MoSe_2$ is evaluated by the degradation of tetraethylated rhodamine (rhodamine B, RhB) solution under visible light irradiation (>420 nm). A bulk $MoSe_2$ particle and a commercial TiO_2 (Degussa P25) were used as references. The initial concentration of RhB solution was 200 ppm. Before light irradiation, the mixture was kept in the dark for 3 h to build up sorption equilibrium. The bulk $MoSe_2$ sample and TiO_2 sample do not show noticeable sorption of RhB, which can be ascribed to their small specific surface areas. The adsorption of RhB onto the mesoporous $MoSe_2$ proceeds quite fast, which is close to saturation within 20 min and reaches equilibrium within 40 min (**Figure 5**a). The adsorption amount of RhB on the mesoporous materials is approximately

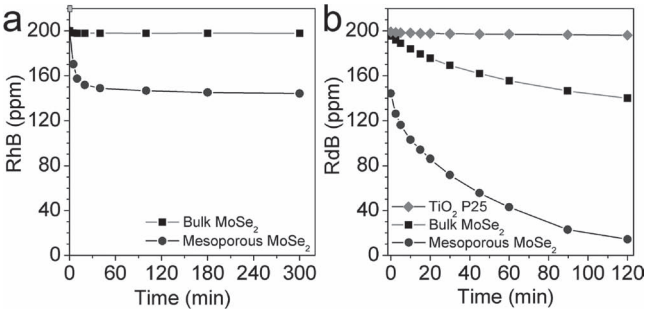

Figure 5. a) The sorption kinetics of RhB onto the bulk $MoSe_2$ particles and the mesoporous $MoSe_2$ material. b) The photodegradation of RhB aqueous solution for mesoporous $MoSe_2$, bulk $MoSe_2$ and TiO_2 (P25) under visible light irradiation (>420 nm).

56 mg g^{-1}, which is quite a high value considering the pore volume of mesoporous $MoSe_2$ is only 0.12 cm^3 g^{-1}. In this case, the significant adsorption of RhB onto the mesoporous $MoSe_2$ decreased the concentration of the RhB solution from 200 to 144 ppm as shown in Figure 5a,b.

Figure 5b shows the time profiles of the concentration of RhB under visible light irradiation for the mesoporous $MoSe_2$ sample, bulk $MoSe_2$ particle and TiO_2. After exposure to visible light, TiO_2 do not show any noticeable catalytic activity because of its large band-gap inhibit its absorption of visible light as reported in numerous papers. In case of bulk $MoSe_2$ and mesoporous $MoSe_2$, the concentration of RhB decreases with the irradiation time, indicating the visible light-driven catalytic decomposition of RhB. The narrow band-gap semiconductor nature of $MoSe_2$ endues the strong absorption of visible light irradiation, which is critical to the visible-light-driven photocatalytic reaction. The first-order linear relationship was revealed by the plots of the $\ln(C/C_0)$ versus irradiation time (t) in both cases (Supporting Information Figure S6). The reaction rate constant k was calculated to be 0.019 and 0.0028 min^{-1} for mesoporous $MoSe_2$ and bulk $MoSe_2$ via the first order linear fit. This result confirms that both mesoporous $MoSe_2$ and bulk $MoSe_2$ possess visible-light-driven photocatalytic activities, and the mesoporous material was 6.8 times as active as the bulk counterpart. The much higher activity of mesoporous $MoSe_2$ can be attributed to that the mesoporosity provides a large surface area and pore volume, which enables RhB molecular adsorption inside the mesopore with a good contact to the $MoSe_2$ catalytic framework.

4. Lithium Storage Performance

Electrochemical lithium storage behavior for the ordered mesoporous $MoSe_2$ was investigated using galvanostatic discharge-charge experiments. **Figure 6**a shows the first three discharge/charge profiles of the mesoporous $MoSe_2$ electrode at a current rate of 0.05 C (0.05 C refers to 4 mol Li uptake into $MoSe_2$ per formula unit in 20 h) between 0.01 and 3.00 V. The shape of the discharge/charge profiles is very similar to those of mesoporous MoS_2, indicating a similar electrochemical storage mechanism, which can be attributed to their similar crystal structure and chemistry properties. The initial discharge and charge capacities of the mesoporous $MoSe_2$ electrode are 759 and 600 mAh g^{-1}, respectively. The irreversible capacity of 159 mAh g^{-1} in the initial cycle is probably due to the formation of a solid electrolyte interface (SEI) layer. It is worth noting that the reversible capacity exceeds the expected theoretical capacity of 422 mAh g^{-1} (assuming an uptake of 4 mol of Li into 1 mol of $MoSe_2$ species). The excess capacity seems to be a normal but highly desirable phenomenon in those layer-structured materials. For example, the theoretical capacity of MoS_2 is 670 mAh g^{-1}, while the nanostructured MoS_2 shows reversible capacity values as high as 750,[48] 800,[50] 850,[49] and even higher than 900 mAh g^{-1}.[45,47,52,54] This might be due to the interfacial Li storage proposed by Maier and/or other reasons which are not clear at this moment.[59]

Although the discharge/charge capacity of mesoporous $MoSe_2$ is much higher than its theoretical capacity value, it still

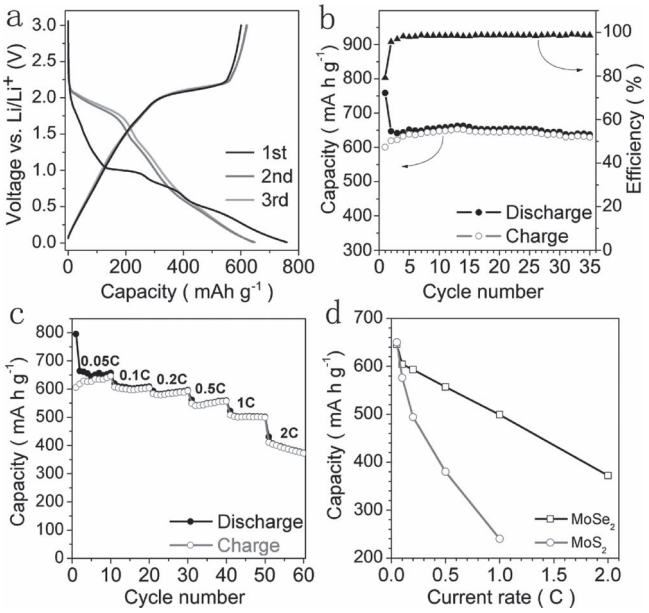

Figure 6. a) The discharge/charge curves of the first three cycles for the mesoporous $MoSe_2$ electrode at a current rate of 0.05 C between 0.01 and 3.00 V. b) Cycling performance of the mesoporous $MoSe_2$ electrode at a current rate of 0.05 C. c) Rate performance of the mesoporous $MoSe_2$ electrode between 0.01 and 3.00 V. d) Comparison of the rate performance between mesoporous $MoSe_2$ and MoS_2 electrodes.

possesses an excellent cycling performance. Figure 6b shows the cycling performance of the mesoporous $MoSe_2$ electrode between 0.01 and 3.00 V at a current rate of 0.05 C. The reversible capacity is stable at 630 mAh g^{-1} after 35 cycles. Although the initial coulombic efficiency is about 79.2%, it increases to 95.7% in the second cycle and remains higher than 98.5% after the fourth cycle. Note that an excellent cycling performance was also obtained at a current rate of 0.1 C as shown in Figure S7 (Supporting Information). This stable cycling performance could be ascribed to the structural stability of the mesoporous $MoSe_2$ electrodes during cycling as shown in Figure S10 (Supporting Information) where the morphologies of the sample can be maintained well though the particle size increases slightly after Li insertion.

Another appealing property of the mesoporous $MoSe_2$ electrode is its superior rate performance comparing to its analogue nanocasting synthesized mesoporous MoS_2 material. Figure 6c shows the rate performance of the mesoporous $MoSe_2$ electrode between 0.01 and 3.00 V. When the discharge/charge rate increases from 0.05 C to 0.1, 0.2, 0.5, 1, and 2 C, the capacity slowly decreases from 646 to 604, 593, 557, 499, and 372 mAh g^{-1}, which is much better than those values reported for mesoporous MoS_2 electrode and microsized $MoSe_2$ electrode as shown in Figure 6d and Figure S8 (Supporting Information), respectively.[60] In the case of mesoporous MoS_2, when the discharge/charge rate increases from 0.05 C to 0.1, 0.2, 0.5, and 1 C, the capacity decreases from 650 to 576, 494, 380, and 240 mAh g^{-1}.[60] The capacity at 1 C of mesoporous $MoSe_2$ (499 mAh g^{-1}) is twice that of MoS_2 (240 mAh g^{-1}). Since the mesoporous $MoSe_2$ possess similar particle size and morphology, pore size, pore volume, surface area, and even nanorod diameter as the mesoporous MoS_2,[60] the enhanced rate performance must be attributed to the electrochemical nature of $MoSe_2$ and better kinetics. Li_2Se and Li_2S are believed to be intermediates during the discharge/charge cycling.[46,60] Therefore, we believe the much higher electric conductivity of Li_2Se might be largely responsible, because the higher electric conductivity would be beneficial for the conversion reaction.

5. Conclusions

We successfully prepared a highly ordered mesoporous crystalline $MoSe_2$ material via a nanocasting method using selenium powder and PMA as Se and Mo sources, respectively. The obtained products possess highly ordered hexagonal arrangement mesostructure and rod-like particle morphology, analogous to its mother template SBA-15. UV-vis-IR spectrum of the mesoporous $MoSe_2$ material shows strong light adsorption in the entire visible light range and its band-gap is estimated to be 1.37 eV. As a result it shows remarkable photocatalytic activity for the degradation of organic compound in aqueous solution under visible light irradiation. In addition, the synthesized mesoporous $MoSe_2$ possess a reversible lithium storage capacity of 630 mAh g^{-1} for up to 35 cycles without any notable decrease. The rate performance of mesoporous $MoSe_2$ is much better than that of mesoporous MoS_2, making it a promising anode candidate for lithium ion battery.

6. Experimental Section

Synthesis of Hard Template SBA-15: 20 g of triblock copolymer P123 was dissolved in a mixture of 600 mL 2M HCl and 150 mL H_2O at 38 °C. Then 41.6 g of TEOS was poured into the solution with rigorously stirring, and the mixture was kept at the same temperature for another 24 h. The above mixture was then transferred into a Teflon lined stainless steel autoclave and heated up to 110 °C for 2 days for hydrothermal treatment. The white solids were recovered by filtration and calcined at 400 °C for 2 h with a heating rate of 1.5 °C min^{-1} in air to remove the P123 surfactant.

Synthesis of Mesoporous $MoSe_2$ Materials: 3.5 g of PMA was mixed with 1 g of SBA-15 and 10 mL of ethanol under stirring in an open crucible at room temperature. After the ethanol was evaporated up after about 5–8 h, the obtained powder was loaded on a quartz boat and putted in the middle of a quartz tube furnace. Another quartz boat that loaded with 4 g of selenium powder was also placed in the tube furnace in the upstream direction just by the side of PMA@SBA-15 boat. Then the furnace was heated to 600 °C at a rate of 2 °C min^{-1} under a hydrogen gas flow (200 mL min^{-1}). After keeping in this temperature for 6 h, the furnace was cooled down to room temperature. The H_2Se in the off gas was absorbed by 2 M NaOH aqueous solution. The obtained $MoSe_2$@SBA-15 composite was treated by 4% HF aqueous solution for 2 h to remove the silica template.

Characterization: XRD patterns were collected on a Scintag PADX diffractometer with Cu Kα radiation (45 kV, 35 mA). TEM images were taken using a FEI Tecnai T20 Sphera electron microscope operating at 200 keV. SEM images were acquired on a FEI XL30 Sirion FEG Digital Scanning electron microscope. Nitrogen sorption isotherms were measured at 77 K on a Micromeritics Tristars 3000 analyzer (USA). Before the measurements, the samples were outgassed at 160 °C in vacuum for 6 h. The Brumauer-Emmett-Teller (BET) method was utilized to calculate the specific surface areas. The pore-size distributions were derived from the adsorption branches of the isotherms using the Barrett-Joyner-Halanda (BJH) method. The total pore volumes, V_p, were

estimated from the amount adsorbed at a relative pressure of P/P_0 = 0.98.

The photocatalytic degradation of tetraethylated rhodamine (RhB) in aqueous solution was carried out in a quartz beaker at room temperature. A 350 W Xe-lamp with a UV cut-off filter ($\lambda > 420$ nm) was used as the visible light source. In each batch of experiment, 200 mg of mesoporous $MoSe_2$ materials was mixed with 200 mL of 200 ppm RhB aqueous solution under stirring. Prior to light irradiation, the reactor was left in the dark for three hour until an adsorption-desorption equilibrium was established. The suspension was magnetically stirred during the sorption in dark and light irradiation.

The working electrode was prepared by casting a slurry of the active material (80 wt%), carbon black (10 wt%) and polyvinylidene fluoride (10 wt%) dissolved in *N*-methylpyrrolidone as the binder on a clean stainless steel grid current collector. Button-type test cells were assembled with mesoporous $MoSe_2$ or MoS_2 or microsized $MoSe_2$ (see SEM image in Supporting Information Figure S9) as the working electrode and fresh Li foil as the counter electrode in an Ar-filled glove box (MBraun, Lab Master 130). The electrolyte was 1 M $LiPF_6$ in ethylene carbonate (EC) and dimethyl carbonate (DMC) (1:1 in volume) and Celgard 2400 was used as the separator. The electrochemical performances were characterized on Land BT 2000 battery tester (Wuhan, China) at room temperature. After the electrochemical test, the cells were disassembled in the Ar-filled glove box and the electrodes were rinsed by DMC and dried in the vacuum chamber connected with glove box. Then the electrodes were subjected to SEM observation through a vacuum transfer box into SEM sample holder without air exposure.

Supporting Information

Supporting Information is available from the Wiley Online Library or from the author.

Acknowledgements

This work was supported by funding from NSFC (21103038, 50972164, 51222210, 21173190), Zhejiang Provincial NSFC (Y4110369), Key Project of Chinese Ministry of Education (211066), the Special Funds for key innovation team of Zhejiang Province (2010R50017), the International Science and Technology Cooperation Program of China (2012DFG42100), the "863" Project (2009AA033101), the 100 Talent Project of the Chinese Academy of Sciences and United States NSF (DMR08-05148) as well as the WCU (World Class University) program through the Korea Science and Engineering Foundation funded by the Ministry of Education, Science and Technology of Korea (R32-2009-000-20074-0).

Received: July 30, 2012
Revised: September 12, 2012
Published online: October 30, 2012

[1] M. E. Davis, *Nature* **2002**, *417*, 813.
[2] Y. Wan, D. Y. Zhao, *Chem. Rev.* **2007**, *107*, 2821.
[3] a) I. I. Slowing, J. L. Vivero-Escoto, C. W. Wu, V. S. Y. Lin, *Adv. Drug Delivery Rev.* **2008**, *60*, 1278; b) F. Zhang, G. B. Braun, A. Pallaoro, Y. C. Zhang, Y. F. Shi, D. X. Cui, M. Moskovits, D. Y. Zhao, G. D. Stucky, *Nano Lett.* **2012**, *12*, 61; c) B. J. Scott, G. Wirnsberger, G. D. Stucky, *Chem. Mater.* **2001**, *13*, 3140.
[4] Y. F. Shi, Y. Wan, D. Y. Zhao, *Chem. Soc. Rev.* **2011**, *40*, 3854.
[5] S. Bag, P. N. Trikalitis, P. J. Chupas, G. S. Armatas, M. G. Kanatzidis, *Science* **2007**, *317*, 490.
[6] M. G. Kanatzidis, *Adv. Mater.* **2007**, *19*, 1165.
[7] J. L. Mohanan, I. U. Arachchige, S. L. Brock, *Science* **2005**, *307*, 397.
[8] P. V. Braun, P. Osenar, S. I. Stupp, *Nature* **1996**, *380*, 325.
[9] P. V. Braun, P. Osenar, V. Tohver, S. B. Kennedy, S. I. Stupp, *J. Am. Chem. Soc.* **1999**, *121*, 7302.
[10] P. V. Braun, P. Osenar, M. Twardowski, G. N. Tew, S. I. Stupp, *Adv. Funct. Mater.* **2005**, *15*, 1745.
[11] C. R. Lubeck, T. Y. J. Han, A. E. Gash, J. H. Satcher, F. M. Doyle, *Adv. Mater.* **2006**, *18*, 781.
[12] P. N. Trikalitis, K. K. Rangan, T. Bakas, M. G. Kanatzidis, *Nature* **2001**, *410*, 671.
[13] P. N. Trikalitis, K. K. Rangan, T. Bakas, M. G. Kanatzidis, *J. Am. Chem. Soc.* **2002**, *124*, 12255.
[14] G. S. Armatas, M. G. Kanatzidis, *Nat. Mater.* **2009**, *8*, 217.
[15] A. H. Lu, F. Schuth, *Adv. Mater.* **2006**, *18*, 1793.
[16] M. Tiemann, *Chem. Mat.* **2008**, *20*, 961.
[17] H. F. Yang, D. Y. Zhao, *J. Mater. Chem.* **2005**, *15*, 1217.
[18] W. B. Yue, W. Z. Zhou, *Prog. Nat. Sci.* **2008**, *18*, 1329.
[19] F. Gao, Q. Y. Lu, D. Y. Zhao, *Adv. Mater.* **2003**, *15*, 739.
[20] X. Y. Liu, B. Z. Tian, C. Z. Yu, B. Tu, Z. Liu, O. Terasaki, D. Y. Zhao, *Chem. Lett.* **2003**, *32*, 824.
[21] Y. F. Shi, Y. Wan, R. L. Liu, B. Tu, D. Y. Zhao, *J. Am. Chem. Soc.* **2007**, *129*, 9522.
[22] R. Coehoorn, C. Haas, J. Dijkstra, C. J. F. Flipse, R. A. Degroot, A. Wold, *Phys. Rev. B* **1987**, *35*, 6195.
[23] R. Coehoorn, C. Haas, R. A. Degroot, *Phys. Rev. B* **1987**, *35*, 6203.
[24] J. Gobrecht, H. Tributsch, H. Gerischer, *J. Electrochem. Soc.* **1978**, *125*, 2085.
[25] G. Kline, K. Kam, D. Canfield, B. A. Parkinson, *Sol. Energy Mater.* **1981**, *4*, 301.
[26] D. Canfield, B. A. Parkinson, *J. Am. Chem. Soc.* **1981**, *103*, 1279.
[27] V. M. Pathak, K. D. Patel, R. J. Pathak, R. Srivastava, *Sol. Energy Mater. Sol. Cells* **2002**, *73*, 117.
[28] B. Zhang, X. C. Ye, W. Y. Hou, Y. Zhao, Y. Xie, *J. Phys. Chem. B* **2006**, *110*, 8978.
[29] Q. T. Wang, X. B. Wang, W. J. Lou, J. C. Hao, *New J. Chem.* **2010**, *34*, 1930.
[30] F. Cao, W. Q. Liu, L. Zhou, R. P. Deng, S. Y. Song, S. Wang, S. Q. Su, H. Zhang, *Solid State Sci.* **2011**, *13*, 1226.
[31] J. Chen, N. Kuriyama, H. Yuan, H. T. Takeshita, T. Sakai, *J. Am. Chem. Soc.* **2001**, *123*, 11813.
[32] J. Chen, F. Wu, *Appl. Phys. A* **2004**, *78*, 989.
[33] J. Chen, S. L. Li, Z. L. Tao, Y. T. Shen, C. X. Cui, *J. Am. Chem. Soc.* **2003**, *125*, 5284.
[34] D. W. Murphy, F. A. Trumbore, *J. Cryst. Growth* **1977**, *39*, 185.
[35] P. Lavela, J. Morales, L. Sanchez, J. L. Tirado, *J. Power Sources* **1997**, *68*, 704.
[36] J. Chen, Z. L. Tho, S. L. Li, *Angew. Chem. Int. Ed.* **2003**, *42*, 2147.
[37] R. Dominko, D. Arcon, A. Mrzel, A. Zorko, P. Cevc, P. Venturini, M. Gaberscek, M. Remskar, D. Mihailovic, *Adv. Mater.* **2002**, *14*, 1531.
[38] J. Morales, J. Santos, J. L. Tirado, *Solid State Ionics* **1996**, *83*, 57.
[39] D. Ilic, K. Wiesener, W. Schneider, *J. Power Sources* **1985**, *14*, 223.
[40] P. Lavela, M. Conrad, A. Mrotzek, B. Harbrecht, J. L. Tirado, *J. Alloys Compd.* **1999**, *282*, 93.
[41] X. L. Li, Y. D. Li, *J. Phys. Chem. B* **2004**, *108*, 13893.
[42] C. H. Lai, K. W. Huang, J. H. Cheng, C. Y. Lee, W. F. Lee, C. T. Huang, B. J. Hwang, L. J. Chen, *J. Mater. Chem.* **2009**, *19*, 7277.
[43] C. H. Lai, K. W. Huang, J. H. Cheng, C. Y. Lee, B. J. Hwang, L. J. Chen, *J. Mater. Chem.* **2010**, *20*, 6638.
[44] E. Shembel, R. Apostolova, I. Kirsanova, V. Tysyachny, *J. Solid State Electrochem.* **2008**, *12*, 1151.
[45] J. Xiao, D. W. Choi, L. Cosimbescu, P. Koech, J. Liu, J. P. Lemmon, *Chem. Mater.* **2010**, *22*, 4522.
[46] J. Xiao, X. J. Wang, X. Q. Yang, S. D. Xun, G. Liu, P. K. Koech, J. Liu, J. P. Lemmon, *Adv. Funct. Mater.* **2011**, *21*, 2840.

[47] K. Chang, W. X. Chen, L. Ma, H. Li, F. H. Huang, Z. D. Xu, Q. B. Zhang, J. Y. Lee, *J. Mater. Chem.* **2011**, *21*, 6251.
[48] G. D. Du, Z. P. Guo, S. Q. Wang, R. Zeng, Z. X. Chen, H. K. Liu, *Chem. Commun.* **2010**, *46*, 1106.
[49] C. Q. Feng, J. Ma, H. Li, R. Zeng, Z. P. Guo, H. K. Liu, *Mater. Res. Bull.* **2009**, *44*, 1811.
[50] G. H. Guo, J. H. Hong, C. J. Cong, X. W. Zhou, K. L. Zhang, *J. Mater. Sci.* **2005**, *40*, 2557.
[51] H. Hwang, H. Kim, J. Cho, *Nano Lett.* **2011**, *11*, 4826.
[52] H. Li, W. J. Li, L. Ma, W. X. Chen, J. M. Wang, *J. Alloys Compd.* **2009**, *471*, 442.
[53] C. Zhang, H. B. Wu, Z. Guo, X. W. Lou, *Electrochem. Commun.* **2009**, *20*, 7.
[54] S. J. Ding, J. S. Chen, X. W. Lou, *Chem. Eur. J.* **2011**, *17*, 13142.
[55] S. J. Ding, D. Y. Zhang, J. S. Chen, X. W. Lou, *Nanoscale* **2012**, *4*, 95.
[56] D. Y. Zhao, J. L. Feng, Q. S. Huo, N. Melosh, G. H. Fredrickson, B. F. Chmelka, G. D. Stucky, *Science* **1998**, *279*, 548.
[57] J. M. Huang, D. F. Kelley, *Chem. Mater.* **2000**, *12*, 2825.
[58] K. K. Kam, B. A. Parkinson, *J. Phys. Chem.* **1982**, *86*, 463.
[59] J. Jamnik, J. Maier, *Phys. Chem. Chem. Phys.* **2003**, *5*, 5215.
[60] X. P. Fang, X. Q. Yu, S. F. Liao, Y. F. Shi, Y. S. Hu, Z. X. Wang, G. D. Stucky, L. Q. Chen, *Microporous Mesoporous Mater.* **2012**, *151*, 418.